Appl Phys B (2011) 104:439–450
DOI 10.1007/s00340-011-4450-2

Applied Physics B
Lasers and Optics

High-vacuum time-resolved laser-induced incandescence of flame-generated soot

J.M. Headrick · F. Goulay · P.E. Schrader · H.A. Michelsen

Received: 26 October 2010 / Revised version: 9 January 2011 / Published online: 16 March 2011

Abstract We have measured time-resolved laser-induced incandescence of flame-generated soot under high-vacuum conditions (4.1×10^{-6} mbar) at an excitation wavelength of 532 nm with laser fluences spanning 0.06–0.5 J/cm^2. We generated soot in an ethylene/air diffusion flame, introduced it into the vacuum system with an aerodynamic lens, heated it using a pulsed laser with a spatially homogeneous and temporally smooth laser profile, and recorded LII temporal profiles at 685 nm. At low laser fluences LII signal decay rates are slow, and LII signals persist beyond the residence time of the soot particles in the detection region. At these fluences, the temporal maximum of the LII signal increases nearly linearly with increasing laser fluence until reaching a plateau at ∼0.18 J/cm^2. At higher fluences, the LII signal maximum is independent of laser fluence within experimental uncertainty. At these fluences, the LII signal decays rapidly during the laser pulse. The fluence dependence of the vacuum LII signal is qualitatively similar to that observed under similar laser conditions in an atmospheric flame but requires higher fluences (by ∼0.03 J/cm^2) for initiation. These data demonstrate the feasibility of recording vacuum LII temporal profiles of flame-generated soot under well-characterized conditions for model validation.

1 Introduction

Laser-induced incandescence (LII) is extensively used to characterize soot in various combustion environments [1–20]. This technique involves heating soot with a laser pulse and recording the resulting blackbody emission. The intensity of the incandescence is used to measure the soot volume fraction, and the decay rate of the LII signal after the laser pulse provides information about the primary-particle size [21–23]. The temporal evolution of the LII signal strongly depends on the laser spatial and temporal profiles [10, 13, 24–28], temporal and spectral response of the detection system [12, 14, 27, 29–33], and ambient pressure [31, 34–40]. Although LII remains a very promising technique to characterize and quantify soot, reliable application under a wide range of combustion environments requires a better understanding of the underlying physical mechanisms and an appreciation of how experimental factors influence signal generation.

Models have been developed to reproduce and predict the temporal profile of soot emission over a wide range of laser fluences [23, 41]. These models solve the mass- and energy-balance equations during and after the laser pulse by considering the most important physical and chemical processes expected to occur during laser heating and subsequent cooling. Mechanisms considered include laser absorption, radiative and conductive cooling, sublimation, nonthermal ablation, phase-changes, and surface chemistry. Predictions from these models have been compared with experimental LII profiles from soot generated in diffusion and premixed flames [25, 28, 30, 42–50]. Specific models have also been developed to predict the LII signal evolution under more extreme environments, such as very dense media [51, 52], high-pressure environments [35, 37, 39, 40], and high-vacuum conditions [34, 36, 38]. Nevertheless, large uncertainties in predicting LII signals still remain. The most significant of these uncertainties stem from an incomplete understanding of mass-loss processes [23, 53–56], conductive cooling [23, 50, 57–59], and temperature and wavelength dependencies of the soot optical properties [27, 60, 61].

J.M. Headrick · F. Goulay · P.E. Schrader · H.A. Michelsen (✉)
Sandia National Laboratories, P.O. Box 969, MS 9055,
Livermore, CA 94551, USA
e-mail: hamiche@sandia.gov

The development of LII as a quantitative tool for soot characterization requires a better understanding of these phenomena. Narrowing these uncertainties will require careful studies of LII data obtained under broad and very well controlled experimental conditions.

A theoretical study by Liu et al. [38] predicts that, after the laser pulse, conductive cooling can be neglected at pressures below 0.1 mbar as long as the particle temperature remains below 2800 K. At these pressures and temperatures, the decay rate of the LII signal is independent of the primary-particle size and is governed by the absolute value of the refractive-index function. By greatly reducing the influence of conductive cooling, vacuum LII experiments allow us to study processes that, under atmospheric conditions, occur on timescales that are competitive with conductive cooling.

Several experimental investigations [34, 36, 62] have reported LII spectral and temporal profiles under low enough pressure that conductive cooling can be neglected. The study by Beyer and Greenhalgh [36] is the most comprehensive in that they characterized the laser-spatial profile and particle-size distribution. Carbon black, with a primary-particle size of 15 nm, was placed in a rotating sealed glass vessel at low pressure ($< 1 \times 10^{-4}$ mbar) and irradiated by a 532-nm laser pulse. The observed single-shot LII temporal profiles do not decrease monotonically and demonstrate a significant increase in signal at long delay times after the laser pulse. The averaged LII profiles, however, do decrease monotonically. The authors attribute the abnormal single-shot temporal behavior to fragmentation of very large aggregates (> 100 µm) after the laser pulse. Soot temperature profiles predicted by a model of the experiment deviated from temperature profiles inferred from the averaged experimental traces collected at two detection wavelengths. These differences could be due to the very large particle aggregate size (>100 µm), which is 3 orders of magnitudes greater than the aggregate size typically measured for soot particles in combustion environments [37, 49, 63–66]. The authors acknowledge that the use of a glass vessel is not optimum to record LII and suggest the use of an aerosol concentrator (aerodynamic lens, ADL) [67–70]. Although the study of Beyer and Greenhalgh [36] experimentally demonstrates the feasibility of LII under high vacuum, it does not provide suitable data for model validation at these low pressures.

Validation of LII models under high vacuum requires an experimental setup with extremely well characterized soot, laser, and detection parameters. In the present work, we demonstrate that an ethylene diffusion flame combined with an ADL [67–70] can be used for time-resolved measurements of LII profiles at pressures of 4.1×10^{-6} mbar. We irradiated the particle beam emanating from the ADL with a pulsed 532-nm laser over a range of laser fluences spanning from 0.06 to 0.50 J/cm^2. We recorded LII temporal profiles under vacuum during and up to 3 µs after the laser pulse with sub-nanosecond time resolution. In this work, we established proper flame operating conditions by monitoring the effects of fuel and air coflow volumetric flow rates on vacuum LII signal. In addition, in the present paper we compare the laser-fluence dependence of the peak of the vacuum-LII signal with LII data recorded at atmospheric pressure in a Santoro burner [61, 63, 64, 71].

2 Experimental

2.1 Vacuum system

The vacuum system implemented in this work (Fig. 1) consists of three differentially pumped chambers, which we designate as the source, detection, and evacuation chambers. Flame-generated soot enters the source chamber by means of an aerodynamic lens (ADL), which for alignment purposes, is attached to a gimbaled bellows nipple allowing adjustments in X, Y, Z, tip, and tilt. The ADL used in these experiments was developed using a design tool created by Wang and McMurry [70], which allows users to model multiple cylindrically symmetric lens elements in series at various user-defined locations and conditions. A cross-sectional schematic drawing of this ADL is displayed in Fig. 2 with critical dimensions shown in Table 1. According to the design tool, this ADL will effectively transmit 94–100% of soot-particles that are sized 30–1000 nm in diameter. The critical orifice mounted to the ADL entrance operates under choked-flow conditions, yielding an approximate sample volumetric-flow rate of 160 sccm (standard cubic centimeters per minute). The gas load presented by the ADL is pumped away by a 1380 l/s turbo molecular pump (Pfeiffer TMU 1600M C). An 8517 l/min dry roots blower (Alcatel ADS 501) backs the source turbo pump and the turbo pumps attached to the detection and evacuation chambers. The base pressure in the source region is 3.3×10^{-9} mbar, but when under gas load the operating pressure is consistently at 2.9×10^{-3} mbar.

Approximately 55 mm past the ADL exit nozzle the particle beam enters and traverses axially through a 55-mm-long particle baffle (see Fig. 3). The baffle terminates at a 2-mm flat open aperture, allowing particles to flow from the source chamber and into the detection chamber. The baffle system is a protective measure that safeguards the source turbo pump from damage caused by heavy particle loading. Such particle loading occurs if the ADL beam is significantly divergent, and a substantial portion of the soot stream does not clear the 2-mm aperture. The stacked V-shaped veins attached to the particle baffle capture the majority of soot particles scattering from the aperture walls, effectively reducing the number of free particles entering the source chamber. Capturing and maintaining soot particles in the source

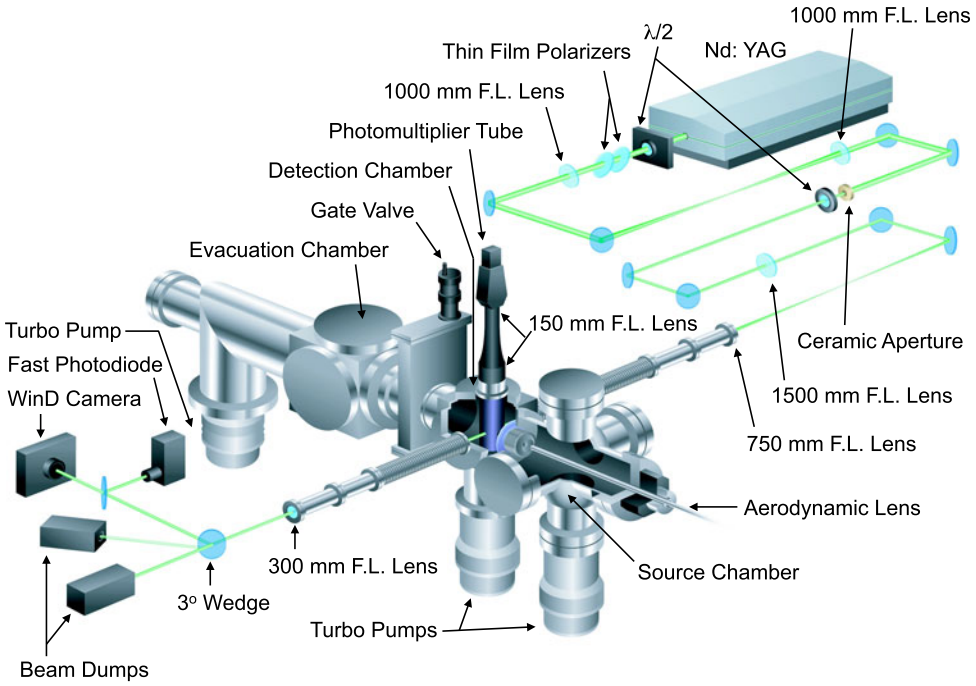

Fig. 1 Schematic diagram of the experimental set-up

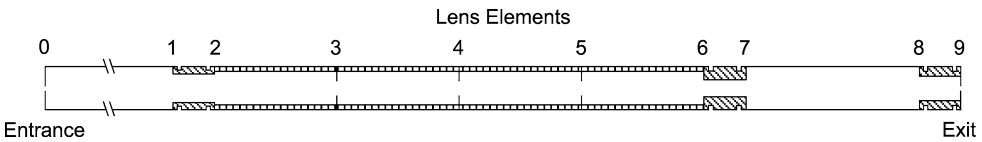

Fig. 2 Schematic diagram of the aerodynamic lens used in this work. The numbers denote locations of different focusing elements within the aerodynamic lens. Focusing elements are defined by the orifice size, tube length after the element, and tube diameter. Dimensions of these focusing elements are given in Table 1

Table 1 Critical dimensions describing the aerodynamic lens shown in Fig. 2

Element:	0	1	2	3	4	5	6	7	8	9
Diameter (mm)	0.152	7.11	7.11	2.99	2.00	1.60	4.04	4.04	6.04	0.78
Tube L. (mm)	441	10.15	49.8	49.8	49.8	49.8	10.14	76.18	9.65	
Tube D. (mm)	10.34	7.11	8.82	8.82	8.82	8.82	4.04	10.34	6.04	

chamber does not significantly affect the base pressure or disrupt the ensuing LII measurement. Future iterations of the particle baffle will replace the 2-mm flat aperture with a conical skimmer of identical open aperture.

After entering the detection chamber, the soot beam travels ∼80 mm (190 mm from the ADL exit nozzle) before entering the detection region where it is crossed orthogonally by the laser beam. Gaining laser access to the detection chamber involves using a 750-mm focal length (FL) imaging lens as the entrance window. Another lens (300-mm FL) for imaging the beam onto the profiler is used as the exit window. The entrance and exit lenses are mounted onto long bellows arms, allowing for full X, Y, Z, tip, and tilt manipulation. Once positioned, the bellows arms are locked down to the adjoining laser tables on either side of the vacuum system.

The bellows arms also shield the LII detector from laser scatter emanating from the entrance and exit lenses. To further protect the detector from laser scatter, a black anodized light baffle is affixed to the top flange of the detection chamber and positioned along the LII collection axis (orthogonal to the laser/soot beam interaction plane, see Fig. 4). The light baffle is a cylindrical shield that extends from the LII optical access port to below the laser interaction plane. The baffle's sealed base and small access ports effectively protect the detector from laser light scattering from the chamber walls. Sealing the detection chamber at the LII optical access port is a 150-mm FL collection lens.

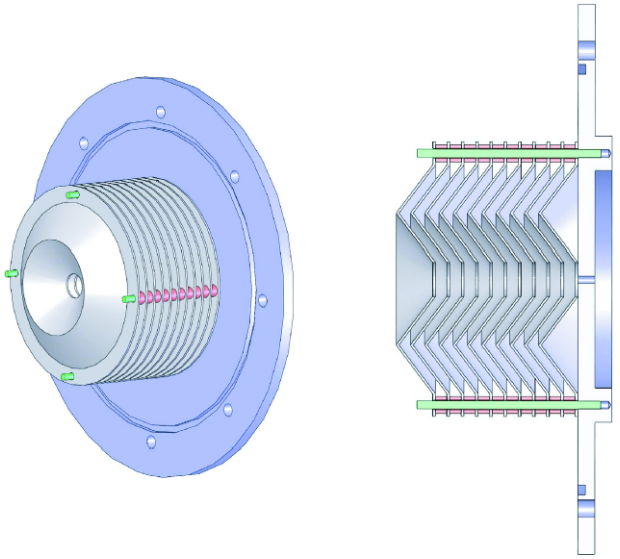

Fig. 3 Profile (*left*) and cutaway (*right*) schematic diagrams of the particle baffle implemented in the source chamber. The particle stream enters the baffle from the *left side*, as represented in this schematic diagram, and passes through the 2-mm aperture that acts as the boundary between the source and detection chambers

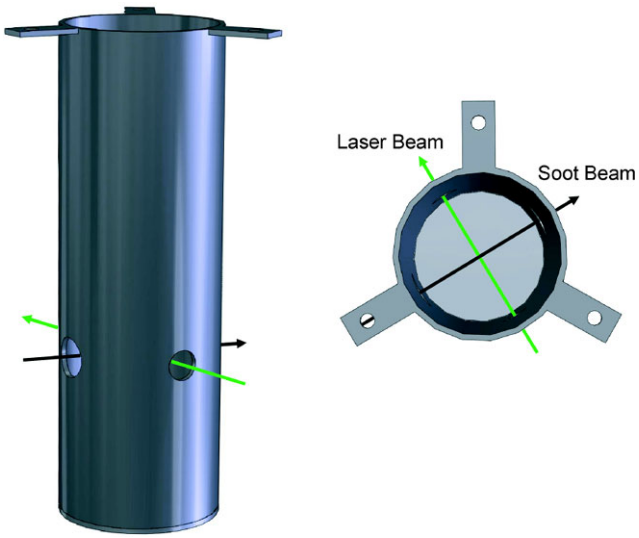

Fig. 4 Schematic diagram of the light baffle surrounding the laser interaction region. The light baffle is mounted to the top flange of the detection chamber, shielding the LII detection optics from scattered laser light reflecting off the chamber walls. The base of the cylindrical tube is sealed, and the entire baffle is anodized black

As with the source chamber, the detection chamber is pumped by a 1380 l/s turbo molecular pump (Pfeiffer TMU 1600M C), but, unlike the source chamber, the base pressure is slightly higher ($\sim 4.0 \times 10^{-8}$ mbar). The higher base pressure is likely due to out gassing of the anodized light baffle and the numerous Viton gaskets used to form seals with the optical components. When acquiring LII signal, the ambient pressure of the detection chamber is constant

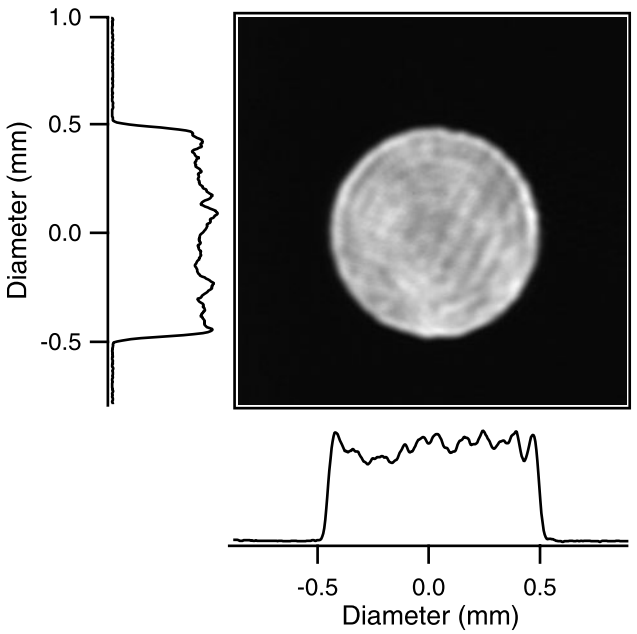

Fig. 5 Spatial beam profile of the apertured laser beam. In this particular example the 1σ standard deviation of the intensity about the mean is 12.6%

at 4.1×10^{-6} mbar. Approximately 280 mm after the laser-interaction region (470 mm from ADL exit nozzle) a 2-mm open aperture allows particles to flow from the detection chamber and into the evacuation chamber.

The evacuation chamber is currently an empty volume that is used solely as a terminus for the particle-beam flight path. At the far-end of this chamber is a particle baffle similar to the one employed in the source chamber, ensuring soot particles colliding with the chamber wall do not escape into the chamber volume and fall into the turbo pump. This chamber is pumped by a 680 l/s turbo pump (Pfeiffer High Pace 700) and achieves a base pressure of 2.6×10^{-9} mbar with an operating pressure of $\sim 1.0 \times 10^{-8}$ mbar.

2.2 Soot generation and characterization

Soot was generated with an ethylene—air diffusion flame using a burner with a central fuel nozzle (5 mm in diameter) surrounded by a honeycomb structure for the air coflow [25, 72]. Fuel and air flow rates were nominally maintained at 282 sccm and 10.7 slm (standard liters per minute) using MKS mass flow controllers (type 1479A for fuel and 1559A for air). At these conditions, the flame height was approximately 100 mm. The entire burner assembly was accommodated into a manifold constructed from NW50 tubing components, with the majority of the flame being housed in a NW50 four-way cross. To prevent complete combustion, one arm of the four-way cross (orthogonal to flame propagation) was equipped with an air stream ($\sim$15 slm, type 1559A MKS mass flow controller), cutting the flame at a height of

64 mm. The air stream was formatted into a pseudo-sheet by reducing the open area of the arm to a circular segment that was only 14% of the original cross-sectional area. The resulting combustion products were allowed to exhaust horizontally down 750 mm of a 47.5-mm-diameter tube (NW50) before the central portion of the gas flow was sampled by a modified piece of 120 mm long, 1/4-inch-diameter stainless steel tubing. The sample stream was flowed through an additional 150 mm of conductive rubber tubing before passing through a stainless steel ball valve and terminating at the ADL entrance nozzle. Exhaust flow temperatures of 120 °C were measured (K-type thermocouple) at the mouth of the sample probe. Rough calculations predicted that the dwell time of gas in the sample line was around three seconds; thus, it can be expected that the sample stream cooled but did not completely thermalize to room temperatures (∼20 °C) prior to ADL extraction.

We used a scanning mobility particle sizer (SMPS) to measure the approximate particle-size distribution of the sampled soot stream. In these experiments, the sample stream going to the ADL was split with a tee and flowed to an electrostatic classifier (EC, TSI Model 3080) equipped with a differential mobility analyzer (DMA, TSI Model 3081). The inlet to the EC was fitted with a single-stage, inertial impactor equipped with a 0.0457-cm diameter nozzle. The monodispersed flow exiting from the DMA was sent to a condensation particle counter (CPC, TSI Model 3010D) for analysis. The volumetric flow rate through the CPC was internally fixed with a choked critical orifice; thus, achieving adjustable sample flow rates through the EC/DMA required a tee and needle relief valve to be attached to the CPC inlet. This configuration allowed room air to be bled into the sample flow, lowering the demand through the EC/DMA. A HEPA filter was attached to the needle valve inlet to avoid pulling in particulate matter from the ambient room environment. Sample flow rates through the SMPS ranged from 0.2–0.3 slm with corresponding DMA sheath flow rates an order of magnitude higher.

2.3 Laser and LII detection setup

Figure 1 includes a schematic representation of the optical setup. Laser radiation was generated by doubling the output of an injection-seeded Nd:YAG (Continuum 8020), producing 532 nm pulses at a repetition rate of 20 Hz and a measured full-width at half-max (FWHM) duration of 5.3 ns. The laser was injection seeded to provide a smooth temporal profile; without injection seeding, this multimode laser generates pulses with large intensity fluctuations with sub-nanosecond rise times [27]. Laser fluence and output polarization were controlled by mounting a half-wave ($\lambda/2$) plate followed by two thin-film-polarizers immediately after the Nd:YAG exit. A 1:1 telescope comprised of two 1000-mm FL lenses was used to relay image the smooth near-field spatial profile of the laser beam to a 2-mm ceramic aperture. The aperture was used to spatially filter the collimated beam by only passing the central portion of the beam where the spatial and temporal distributions of the laser pulse were flattest. The final laser polarization was controlled by a half-wave plate mounted immediately after the aperture. The ceramic aperture was relay imaged into the vacuum chamber by a 2:1 telescope using a pair of lenses with focal lengths of 1500 mm and 750 mm. The resulting collimated image plane formed a nominally 1-mm-diameter laser beam that crossed orthogonally to the ADL-prepared flame-generated soot stream. A portion of the laser beam exiting the vacuum system was reflected from a 3° wedged window and reimaged using a single 300-mm FL lens onto a CCD camera with 4.65×4.65 μm resolution (DataRay WinCamD) to profile the beam or a GaAs photodiode (Electro-Optics Technology ET-4000) to monitor the spatio-temporal profile. As shown in Fig. 5, this optical set up generated laser beam profiles that were spatially homogeneous to within 12.5 to 13.6% (1σ standard deviation about the mean) and had a spatio-temporal deviation of less than 0.6 ns [26].

The soot/laser interaction region was imaged onto the 4-mm active area of a 0.79-ns rise-time gated photomultiplier tube (PMT, Hamamatsu R7400U-20) using a 1:1 telescope consisting of a pair of 150-mm FL lenses. The gated PMT collected LII signal for a duration of 21 μs, with the gate opening 2 μs before the Nd:YAG Q-switch was programmed to fire. To eliminate scattered laser light the active area of the PMT was covered with a 3.88-mm diameter iris followed by a pair of 532/1064-nm notch filters (Semrock NF03-532/1064E-25) and a single 685 ± 20 nm bandpass filter (Semrock FF01-685/40-25). Signal collected from the PMT was digitized and saved using a 4 GHz Agilent 80404B oscilloscope, which was optically triggered by a fast InGaAs photodiode (Electro-Optics Technology ET-3500) viewing 1064 nm light inside the Nd:YAG oscillator housing.

3 Results and discussion

3.1 Single-shot data, signal averaging, and ADL performance implications

Figure 6 displays single-shot and averaged vacuum-LII temporal profiles recorded at a laser fluence of 0.178 J/cm^2. The lower panel of Fig. 6 provides an expanded view of the first 200 ns, revealing that the single-shot data consists of a string of single-photon emissions. The limited photoemission suggests that the soot volume fraction provided by the ADL was low and that the laser pulse was interacting with only a few soot particles. Regardless of the low particle densities, each laser shot resulted in recordable signal, which permitted continuous data averaging. The averaged LII waveforms

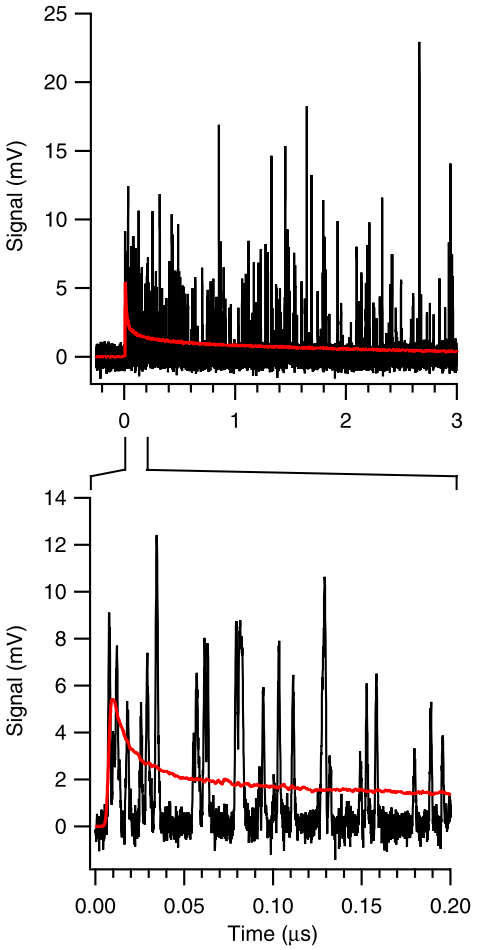

Fig. 6 Single-shot (*black line*) and averaged (*red line*) vacuum-LII data acquired at a laser fluence of 0.178 J/cm^2. The upper panel displays the full time scale, whereas the lower panel expands the first 200 ns, revealing single-photon resolution. The averaged trace is the result of 4 096 laser shots

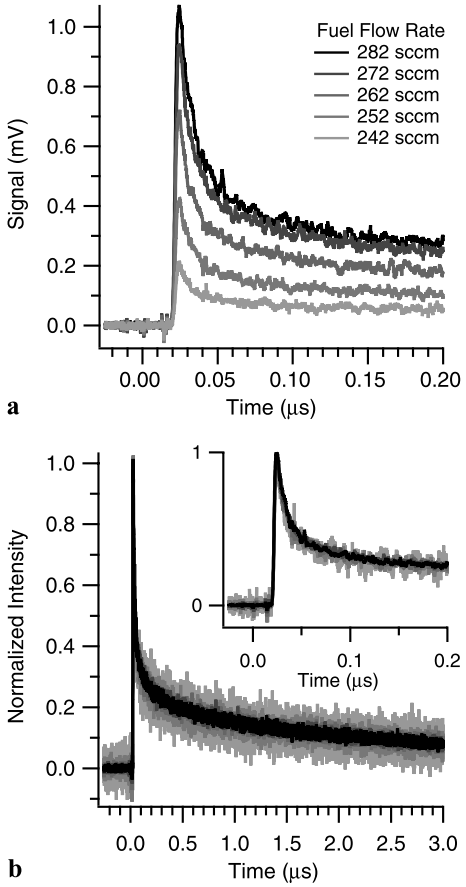

Fig. 7 Absolute (**a**) and normalized (**b**) vacuum-LII waveforms acquired at various ethylene fuel flow rates. The flow rate of the air co-flow for the burner was fixed at 12.6 slm, and the extinguishing air cross-flow rate was held constant at 15.7 slm. The laser fluence was 0.178 J/cm^2 for all measurements

are smooth. Signal-to-noise ratios demonstrated negligible improvement when the number of shots averaged exceeded 4 000, and thus all averaged LII waveforms presented here are the result of a 4 096 laser shot average. The quality of the averaged data shown in Fig. 6 is typical of vacuum-LII waveforms resulting from high averaging.

The signal levels recorded in Fig. 6 were lower than we expected. By comparing our signals with those collected in an atmospheric flame using a similar optical arrangement [73] and known soot volume fraction [65, 71, 74], we infer that our signal levels correspond to ∼3000 primary particles, or ∼30 soot aggregates with an average of 99 primary particles. This value departs significantly from estimates garnered from the ADL design tool, which, when used in conjunction with SMPS data (discussed in Sect. 3.2), predicted the laser-interaction region to be populated by 1000's of soot aggregates. This result suggests that the ADL output experiences substantial beam divergence, which was confirmed when inspecting the vacuum system after an extended period of use. The aperture walls separating the source/detection and detection/evacuation chambers were both imprinted with ∼10 mm soot spots. Using the known separation of the two walls (360 mm), we estimated that the soot beam had a diameter of ∼3.75 mm when traversing the laser-interaction region. This value is much larger than the 1-mm diameter predicted by the ADL design tool. This deviation is likely due to the fact that the ADL design tool does not account for lift forces experienced by non-spherical particles. The beam divergence we experience with our ADL is substantial and needs to be reduced; this goal is reserved for future work.

LII signals persist for durations much longer than what is shown in Fig. 6. The reason for truncating the temporal window is that particle-terminal velocities leaving the ADL are size dependent, with smaller particles traveling at higher velocities than those that are larger. Consequently, dwell times for irradiated particles traveling through the PMT collection window are also size dependent; after ∼4 μs this effect becomes apparent in the LII decay rate. Therefore, we only

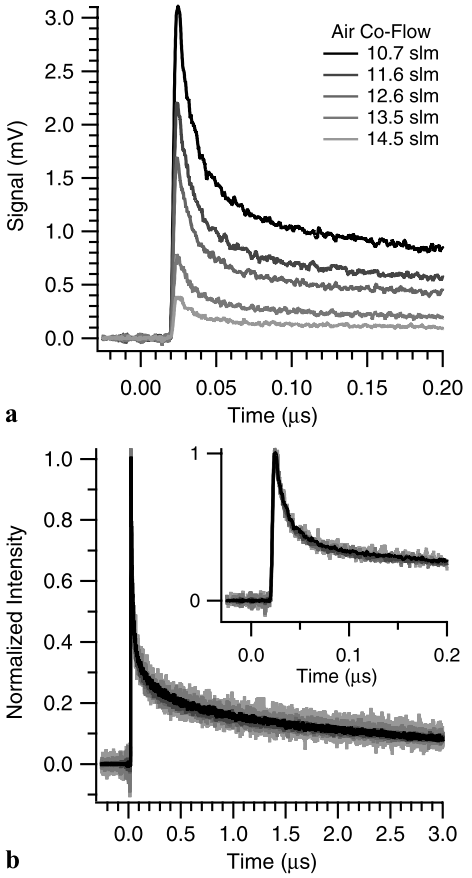

Fig. 8 Absolute (**a**) and normalized (**b**) vacuum-LII waveforms acquired at various diffusion air coflow rates. The ethylene fuel flow rate was fixed at 282 sccm, and the extinguishing air cross-flow rate was fixed at 15.7 slm. The laser fluence was 0.178 J/cm^2 for all measurements

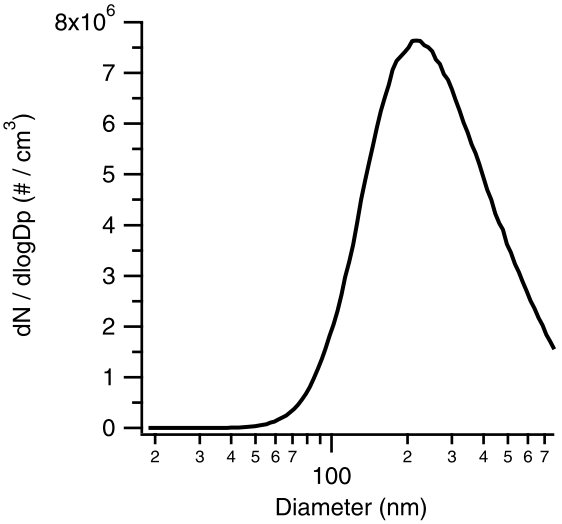

Fig. 9 Electric-mobility-size distribution of flame-generated soot. The particle stream was sampled prior to flowing through the entrance nozzle of the aerodynamic lens. Burner flow rates were 282 sccm for the ethylene fuel, 10.7 slm for the coflow air, and 15.7 slm for the extinguishing cross-flow air

show LII waveforms for durations less than 3 μs, assuring that the displayed averaged waveforms correctly represent the soot distribution sampled. Analysis and interpretation of these waveforms will be presented later in the text.

3.2 Soot characterization, LII flame dependence, and LII stability

To assess how flame conditions affect the probed soot stream, we performed a systematic study by monitoring fuel and air coflow settings as a function of LII signal response. The first set of flame conditions fixed the flow rates for the burner air coflow at 12.6 slm and the air cross-flow at 15.7 slm, while the fuel volumetric flow rate was incrementally decreased. Figure 7 displays the LII data resulting from soot sampled at five different fuel settings between 242 and 282 sccm; the laser fluence was maintained 0.178 J/cm^2. As shown in Fig. 7a, the LII signal decreases with decreasing fuel flow rate, indicating that the sampled soot volume fraction diminishes as the fuel/air mixture becomes leaner. This outcome agrees with expectations because leaner fuel conditions lead to more complete combustion, resulting in less favorable sooting conditions. The normalized LII traces displayed in Fig. 7b demonstrate excellent overlap of the signal decay rates across all flame conditions, lasting throughout the duration of signal acquisition.

In the second set of flame conditions we fixed the fuel flow at 282 sccm and the air cross-flow at 15.7 slm, while soot was sampled at five different air coflow rates ranging from 10.7 to 14.5 slm. The resulting LII data, acquired at a constant laser fluence just under 0.18 J/cm^2, are shown in Fig. 8. In this case, the LII signal decreases as the air coflow is incrementally increased, as depicted in Fig. 8a. This observation is consistent with expectations because increases to the air coflow reduce the global equivalence ratio, yielding leaner fuel/air mixtures and unfavorable sooting conditions. As with the behavior observed for changes in fuel flow rate, the LII decay rate is insensitive to changes in the flow rate of the air coflow, as demonstrated by the overlap of the normalized data shown in Fig. 8b. These results indicate that, when confined to the range of flame conditions discussed above, fuel and air coflow settings do not affect the soot properties dictating the decay of vacuum LII signal.

The data in Figs. 7 and 8 show that highly sooting flame conditions yield higher LII signals with no detectable effect on the LII signal decay rate. Therefore, throughout the remainder of this work we have used flame conditions of 282 sccm for the fuel flow rate, 10.7 slm for the air coflow, and 15.7 slm for the air extinguishing cross-flow rate. To characterize this flame condition, we used an SMPS to measure electric mobility sizes, as described in Sect. 2.2. Figure 9 shows that the soot distribution has a maximum value at an electric-mobility particle size of 217 nm with a FWHM of

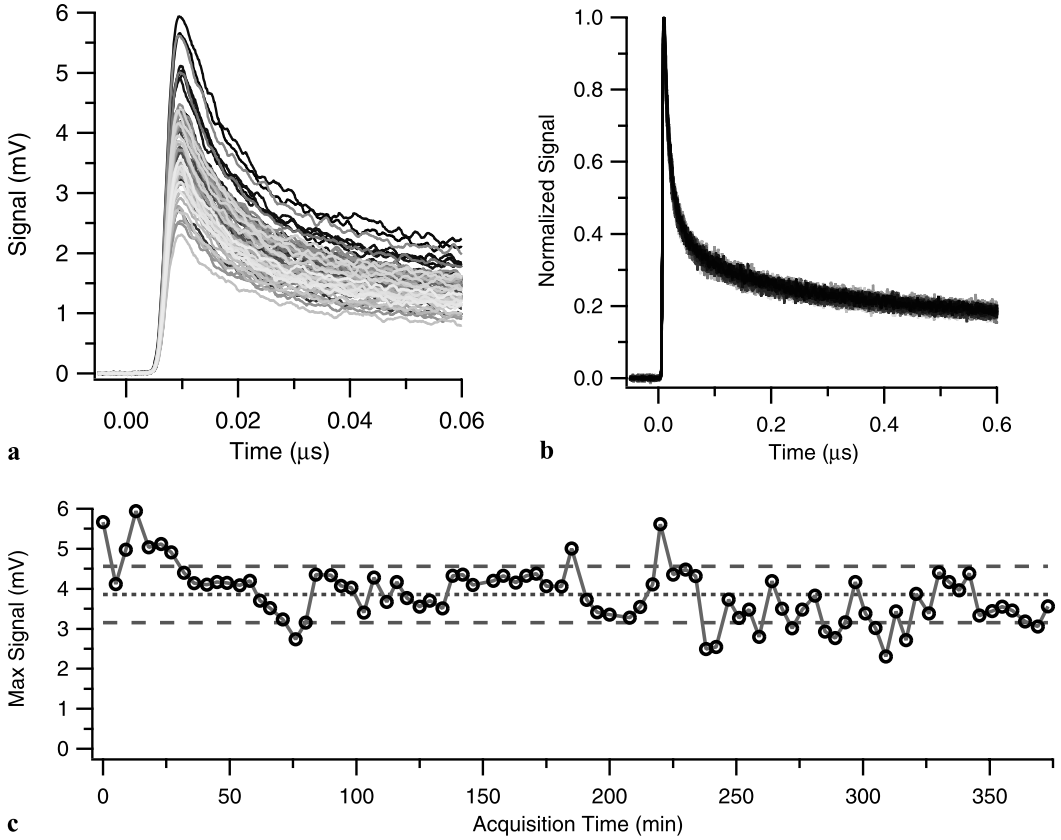

Fig. 10 Flame stability as monitored by LII. The composite plot of all 85 waveforms is depicted in (**a**) with the corresponding normalized data shown in (**b**). The time evolution of the signal maxima is shown in (**c**) with the averaged signal and 1σ deviation denoted by *dotted* and *dashed lines*, respectively. The laser fluence was just under $0.178\ \mathrm{J/cm^2}$ for all measurements

335 nm. The SMPS scan range is truncated at 765 nm because of sampling conditions. SMPS measurements were performed at the various flame conditions discussed previously in this section; however, the SMPS data possessed more inherent variability than could be induced by changes to the flame condition. In order to avoid these issues in the future, we will characterize the ADL soot stream directly by preparing and analyzing transmission electron microscopy (TEM) samples.

In order to assess the long- and short-term stability of the diffusion flame while operating at the optimal flame condition, we collected LII data continuously over many hours. Figure 10 displays the absolute and normalized waveforms for 85 LII temporal profiles collected over the span of 373 minutes at a laser fluence of $0.178\ \mathrm{J/cm^2}$ (laser variability less than $\pm 1\%$). As seen in Fig. 10a, there is a degree of variability in the absolute LII signal intensity, but the normalized data in Fig. 10b show excellent overlap, indicating that the temporal profiles remain unchanged throughout the duration of data acquisition. The time evolution of the LII temporal maximum is shown in Fig. 10c, with time 0 indicating when the flame was ignited. The average signal and 1σ standard deviation is denoted by dashed and dotted lines, and the percent standard deviation for the data set is approximately 18.2%.

Variability in the LII stability dataset (Fig. 10c) does not indicate a statistical necessity for the burner system to endure a prolonged thermal stabilization process. In spite of this, 90 minutes were allocated typically for sample/exhaust lines to achieve complete thermal equilibrium. The flame condition used in these experiments yield large quantities of soot, resulting in significant soot deposits on the sample probe. These deposits may be constricting the sample flow and also causing irregular particle loading of the sample stream, giving rise to occasional signal spikes and inconsistencies in the LII data. Erratic variations observed in Fig. 10c after ~230 minutes are likely due to this type of sample system fouling.

3.3 LII temporal profiles and fluence dependence

We acquired vacuum LII measurements at twenty laser fluences ranging from 0.06 to $0.50\ \mathrm{J/cm^2}$. Waveforms shown in the figures are an average of four measurements, each of which is from an average of 4 096 laser shots. Figures 11 and 12 display LII temporal profiles collected at four laser

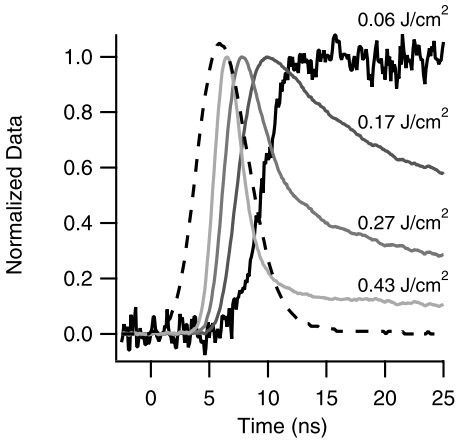

Fig. 11 Normalized vacuum LII temporal profiles at selected laser fluences. LII temporal profiles (*solid lines*) are shown for four laser fluences, as labeled. The peaks of the curves are normalized to a value of one. The laser temporal profile is represented by a *dashed line* and is displayed in arbitrary units

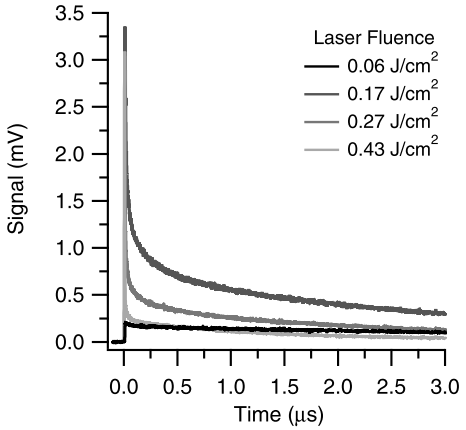

Fig. 12 Vacuum LII temporal profiles at selected laser fluences. The same LII temporal profiles displayed in Fig. 11 are shown here on a time axis expanded to the duration of signal acquisition for selected laser fluences, as labeled. In this figure, the signals have not been normalized

fluences. The temporal evolution of the normalized data during the laser pulse is depicted in Fig. 11, whereas the absolute signal shown over the entire 3-μs collection window is shown in Fig. 12. These LII waveforms are representative of LII temporal profiles in different fluence regimes within the entire fluence range.

The timing amongst the LII profiles, as shown in Fig. 11, is well defined with errors being dictated by the optical trigger jitter; however, the absolute timing of the laser pulse relative to the LII profiles was not directly measured and has been approximated with an estimated uncertainty of 2–3 ns. Sublimation is not expected to be a dominant process at the lowest laser fluence, and the laser energy absorbed by the particle simply raises the temperature of the soot, yielding an increase in LII signal. Radiative cooling occurring during the laser pulse is negligible compared to laser absorption; thus, the particle temperature and LII signal are both at a maximum at the end of the laser. The position of the laser profile in Fig. 11 is determined by matching the maximum of the integrated laser pulse to the LII temporal maximum observed at the lowest laser fluence (0.06 J/cm^2). Figure 12 shows that, at the lowest laser fluence, the signal decays more rapidly during the first 130 ns of data acquisition than at later times, and barely decreases throughout the rest of the 3-μs window. The long-time result is expected as the lack of conductive cooling (because of the high-vacuum environment) [38] and limited particle heating (low laser fluence) allows radiative cooling to be the dominant mode of energy loss, a process inherently slow, and consequently, long-lasting.

At higher fluences (Fig. 11) the LII signal starts to decay before the end of the laser pulse. The fast LII signal decay observed at 0.17 J/cm^2 and 0.27 J/cm^2 is characteristic of fast mass-loss processes similarly observed at atmospheric conditions [12, 27, 33, 55, 61, 75–77]. At nearly the highest fluence (see Fig. 11 at 0.43 J/cm^2), the LII signal exhibits very fast decay rates with 83% of the signal decreasing in 5 ns, a duration that is significantly shorter than the laser pulse. Under atmospheric flame conditions soot particles subjected to high laser fluences will reach sublimation temperatures during the laser pulse, leading to the formation of C, C_2, or C_3 species in the surrounding gas phase [12, 29, 33, 62, 78–82]. A theoretical study by Liu et al. [38] predicted that under vacuum conditions sublimation becomes nonnegligible at temperatures near and above 2800 K, which is much lower than the sublimation temperature of graphite at atmospheric pressures (>4100 K). Other forms of fast mass loss, such as laser ablation [45, 56], can also occur during the laser pulse. For any of these mechanisms, the rate of mass loss increases with increasing laser fluence. Because the LII signal is approximately proportional to the volume (i.e., mass) of the soot primary particle, rapid mass loss leads to fast signal decay rates.

At high fluences, the LII signal continues to decay rapidly after the laser pulse before settling into a characteristic radiative emission signature (see Fig. 12). The LII decays observed well after the laser pulse at high fluence resemble those acquired at low fluence, with the remaining particles cooling radiatively (see Fig. 12). The decay rates at long times are faster at higher fluences than at lower fluences because the radiative emission rate depends on particle temperature, and higher particle temperatures are reached at higher fluences. Because particles that have been irradiated at high fluence have generally experienced significant mass loss and LII signals depend on particle size, these higher-fluence temporal profiles may eventually reach lower signal values than those from lower-fluence temporal profiles at long timescales.

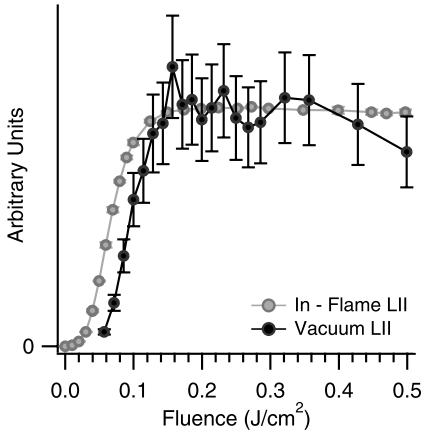

Fig. 13 Fluence dependence of the peak vacuum LII compared to peak LII at atmospheric pressure and flame temperature (∼1660 K). The maximum of the temporal profile of the vacuum LII (*black line* and *symbols*) is shown as a function of fluence in comparison with the maximum of the temporal profile of LII measured in a flame at atmospheric pressure (*gray line* and *symbols*)

Figure 13 displays peak vacuum LII signal and peak atmospheric flame LII signal [61] as a function of laser fluence over the entire experimental fluence range studied here. The error bars for the flame data represent 1σ standard deviation about the mean of three measurements, whereas the errors for the vacuum data represent the 18.2% deviation discussed in Sect. 3.2 of this manuscript. The flame and vacuum data are normalized to the averaged vacuum LII maximum measured between fluences of 0.20 and 0.35 J/cm^2. Under vacuum conditions and at fluences below 0.10 J/cm^2 the peak LII signal increases nearly linearly with increasing fluence. A similar increase in the peak LII signal is observed when recording LII data in an atmospheric ethylene flame and is attributed to an increase of the maximum soot temperature during the laser pulse [12, 29, 45, 61, 83]. The onset and rise of LII signals under vacuum conditions are ∼0.03 J/cm^2 higher than observed in the ethylene flame data. This difference between the vacuum and atmospheric flame data is likely due to the large difference in initial soot temperature (∼1660 K in the flame [71, 84, 85], compared to 300–400 K in the vacuum chamber), with the colder vacuum soot requiring more laser energy to induce observable incandescence emission.

The peak vacuum LII signal is independent of laser fluence above 0.18 J/cm^2 within experimental uncertainties, and the vacuum and atmospheric flame LII temporal maxima appear to reach a plateau at nearly the same laser fluence. Although the error bars on the vacuum data set are large enough to preclude a definitive evaluation of the plateau onset, matching plateau onsets (if real) may be caused by the lower sublimation temperature experienced at high vacuum. Plateaus in the peak LII signal in atmospheric flames correspond to soot temperatures of above 4 100 K [43, 61, 86, 87]. These temperatures are consistent with the sublimation threshold for C, C_2, and C_3 from graphite at atmospheric pressure [87]. Above the sublimation threshold, the energy absorbed by the particles vaporizes the soot without any increase of temperature. This effect is likely occurring in the vacuum LII data, but at a much lower temperature because of the reduced pressure surrounding the particles.

4 Conclusions

We have recorded laser-induced incandescence temporal profiles under vacuum conditions (∼4.1×10^{-6} mbar) for a CW beam of flame-generated soot irradiated with a nanosecond 532-nm laser pulse. The soot-aggregate electric-mobility size distribution was centered at 217 nm with a relatively broad distribution. We performed experiments using a spatially homogeneous 532-nm beam with a smooth temporal profile and spatio-temporal deviations across the beam profile of <0.6 ns. LII temporal profiles were recorded for laser fluences ranging from 0.06 to 0.50 J/cm^2 using a PMT detector with a rise time of 0.79 ns in conjunction with a 40-nm-wide bandpass filter centered at 685 nm. Changing the initial flame conditions affected only the magnitude of the LII signal with no noticeable effect on the shape of the LII temporal profile.

The pressure surrounding the soot was more than four orders of magnitude lower than the predicted pressure below which conductive cooling can be neglected [38]. At the lowest fluences studied sublimation is also believed to be negligible, making radiative cooling the dominant contributor to the LII signal decay. At fluences below 0.10 J/cm^2 the magnitude of the LII signal increased nearly linearly with rising fluence, behavior similar to that observed at atmospheric pressure. As laser fluence increases, the LII temporal profiles demonstrate increasingly fast decay rates during the laser pulse, suggesting fast laser-induced mass-loss processes. Above 0.18 J/cm^{-2} , the peak LII signal is independent of laser fluence within experimental uncertainties. At these fluences, the temperature of the soot under vacuum is likely to achieve a maximum during the laser pulse, as observed when measuring soot temperature under flame conditions. Differences between the vacuum and in-flame LII measurements are demonstrated by the fluence dependence of the LII temporal maximum. The onset and rise of vacuum LII signal, when compared to ethylene flame data, are shifted to higher fluences by 0.03 J/cm^2; this offset is likely due to a lower initial soot temperature in the vacuum chamber (∼300–400 K) than in the flame (∼1660 K [71, 84, 85]).

The experimental setup presented here is suitable for recording time-resolved LII profiles under high-vacuum conditions under well controlled experimental conditions for model comparison. These conditions reduce conductive-cooling contributions and allow other cooling and heating

processes occurring on conductive-cooling timescales at atmospheric conditions to be isolated for study. Future improvements of the experimental setup will involve decreasing ADL divergence, increasing sampling stability, analyzing particles with TEM, measuring the absolute timing of the laser relative to the LII profiles, and making multicolor LII measurements for temperature profiles.

Acknowledgements We thank Daniel Strong for the rendition of the experimental setup shown in Fig. 1. This work was funded by the Division of Chemical Sciences, Geosciences, and Biosciences, the Office of Basic Energy Sciences, the US Department of Energy. Sandia is a multiprogram laboratory operated by Sandia Corporation, a Lockheed Martin Company, for the National Nuclear Security Administration under contract DE-AC04-94-AL85000.

References

1. J.E. Dec, A.O. zur Loye, D.L. Siebers, SAE Transact. **100**, 277 (1991)
2. J.E. Dec, SAE Transact. **101**, 101 (1992)
3. C. Espey, J.E. Dec, Proc. - Soc. Automot. Eng. **102**, 703 (1993)
4. J.A. Pinson, D.L. Mitchell, R.J. Santoro, in *Proc. SAE*, SAE Paper No. 932650 (1993)
5. J.A. Pinson, T. Ni, T.A. Litzinger, SAE Transact. **103**, 1773 (1994)
6. K. Inagaki, S. Takasu, K. Nakakita, SAE Transact. **108**, 574 (1999)
7. D. Snelling, G.J. Smallwood, R.A. Sawchuk, W.S. Neill, D. Gareau, W.L. Chippior, F. Liu, Ö.L. Gülder, SAE Transact. **108**, 2156 (1999)
8. D. Snelling, G.J. Smallwood, R.A. Sawchuk, W.S. Neill, D. Gareau, D.J. Clavel, W.L. Chippior, F. Liu, Ö.L. Gülder, W.D. Bachalo, SAE Transact. **109**, 1914 (2000)
9. P.O. Witze, SAE Transact. **111**, 661 (2002)
10. N.P. Tait, D.A. Greenhalgh, Ber. Bunsenges. Phys. Chem. **97**, 1619 (1993)
11. F. Cignoli, S. Benecchi, G. Zizak, Appl. Opt. **33**, 5778 (1994)
12. R.L. Vander Wal, K.J. Weiland, Appl. Phys. B, Lasers Opt. **59**, 445 (1994)
13. T. Ni, J.A. Pinson, S. Gupta, R.J. Santoro, Appl. Opt. **34**, 7083 (1995)
14. C.R. Shaddix, K.C. Smyth, Combust. Flame **107**, 418 (1996)
15. H. Geitlinger, Th. Streibel, R. Suntz, H. Bockhorn, Combust. Sci. Technol. **149**, 115 (1999)
16. D.J. Bryce, N. Ladommatos, H. Zhao, Appl. Opt. **39**, 5012 (2000)
17. B. Axelsson, R. Collin, P.-E. Bengtsson, Appl. Phys. B, Lasers Opt. **72**, 367 (2001)
18. T. Schittkowski, B. Mewes, D. Brüggemann, PCCP, Phys. Chem. Chem. Phys. **4**, 2063 (2002)
19. M.D. Smooke, M.B. Long, B.C. Connelly, M.B. Colket, R.J. Hall, Combust. Flame **143**, 613 (2005)
20. J.P. Schwarz, R.S. Gao, D.W. Fahey, D.S. Thomson, L.A. Watts, J.C. Wilson, J.M. Reeves, M. Darbeheshti, D.G. Baumgardner, G.L. Kok, S.H. Chung, M. Schulz, J. Hendricks, A. Lauer, B. Karcher, J.G. Slowik, K.H. Rosenlof, T.L. Thompson, A.O. Langford, M. Loewenstein, K.C. Aikin, J. Geophys. Res. **111**, D16207 (2006)
21. R.J. Santoro, C.R. Shaddix, in *Applied Combustion Diagnostics*, ed. by K. Kohse-Höinghaus, J.B. Jeffries (Taylor & Francis, New York, 2002), pp. 252–252
22. C. Schulz, B.F. Kock, M. Hofmann, H.A. Michelsen, S. Will, B. Bougie, R. Suntz, G.J. Smallwood, Appl. Phys. B, Lasers Opt. **83**, 333 (2006)
23. H.A. Michelsen, F. Liu, B.F. Kock, H. Bladh, A. Boiarciuc, M. Charwath, T. Dreier, R. Hadef, M. Hofmann, J. Reimann, S. Will, P.-E. Bengtsson, H. Bockhorn, F. Foucher, K.P. Geigle, C. Mounaïm-Rousselle, C. Schulz, R. Stirn, B. Tribalet, R. Suntz, Appl. Phys. B, Lasers Opt. **87**, 503 (2007)
24. D. Snelling, F. Liu, G.J. Smallwood, Ö.L. Gülder, in *Proceedings of the 34th National Heat Transfer Conference, NHTC2000* (2000)
25. H.A. Michelsen, P.O. Witze, D. Kayes, S. Hochgreb, Appl. Opt. **42**, 5577 (2003)
26. M.A. Dansson, M. Boisselle, M.A. Linne, H.A. Michelsen, Appl. Opt. **46**, 8095 (2007)
27. F. Goulay, P.E. Schrader, H.A. Michelsen, Appl. Phys. B **96**, 613 (2009)
28. H. Bladh, J. Johnsson, P.E. Bengtsson, Appl. Phys. B, Lasers Opt. **96**, 645 (2009)
29. R.L. Vander Wal, Appl. Opt. **35**, 6548 (1996)
30. M. Charwath, R. Suntz, H. Bockhorn, Appl. Phys. B, Lasers Opt. **83**, 435 (2006)
31. H. Bladh, J. Johnsson, P.-E. Bengtsson, Appl. Phys. B **90**, 109 (2008)
32. F. Liu, D.R. Snelling, K.A. Thomson, G.J. Smallwood, Appl. Phys. B **96**, 623 (2009)
33. F. Goulay, P.E. Schrader, L. Nemes, M.A. Dansson, H.A. Michelsen, Proc. Combust. Inst. **32**, 963 (2009)
34. G.S. Eom, C.W. Park, Y.H. Shin, K.H. Chung, S. Park, W. Choe, J.W. Hahn, Appl. Phys. Lett. **83**, 1261 (2003)
35. M.S. Tsurikov, K.P. Geigle, V. Kruger, Y. Schneider-Kuhnle, W. Stricker, R. Luckerath, R. Hadef, M. Aigner, Combust. Sci. Technol. **177**, 1835 (2005)
36. V. Beyer, D.A. Greenhalgh, Appl. Phys. B, Lasers Opt. **83**, 455 (2006)
37. K.A. Thomson, D.R. Snelling, G.J. Smallwood, F. Liu, Appl. Phys. B, Lasers Opt. **83**, 469 (2006)
38. F. Liu, K.J. Daun, V. Beyer, G.J. Smallwood, D.A. Greenhalgh, Appl. Phys. B, Lasers Opt. **87**, 179 (2007)
39. G.B. Kim, J.Y. Shim, S.W. Cho, Y.J. Chang, C.H. Jeon, J. Mech. Sci. Technol. **22**, 1154 (2008)
40. M. Hofmann, F. Kock, T. Dreier, H. Jander, C. Schulz, Appl. Phys. B, Lasers Opt. **90**, 629 (2008)
41. L.A. Melton, Appl. Opt. **23**, 2201 (1984)
42. S. Will, S. Schraml, A. Leipertz, Opt. Lett. **20**, 2342 (1995)
43. S. Schraml, S. Dankers, K. Bader, S. Will, A. Leipertz, Combust. Flame **120**, 439 (2000)
44. Th. Lehre, H. Bockhorn, B. Jungfleisch, R. Suntz, Chemosphere **51** (2003)
45. H.A. Michelsen, J. Chem. Phys. **118**, 7012 (2003)
46. S. Dankers, A. Leipertz, Appl. Opt. **43**, 3726 (2004)
47. H.A. Michelsen, Appl. Phys. B, Lasers Opt. **83**, 443 (2006)
48. H. Bladh, P.-E. Bengtsson, J. Delhay, Y. Bouvier, E. Therssen, P. Desgroux, Appl. Phys. B **83**, 423 (2006)
49. A. Boiarciuc, F. Foucher, C. Mounaim-Rousselle, Appl. Phys. B, Lasers Opt. **83**, 413 (2006)
50. D.R. Snelling, K.A. Thomson, G.J. Smallwood, Appl. Phys. B **96**, 657 (2009)
51. L.H. Chen, A. Garo, K. Cen, G. Grehan, Appl. Phys. B, Lasers Opt. **87**, 739 (2007)
52. R. Ochoterena, Appl. Phys. B, Lasers Opt. **96**, 695 (2009)
53. G.J. Smallwood, D. Snelling, F. Liu, Ö.L. Gülder, J. Heat Transf. **123**, 814 (2001)
54. H. Bladh, P.-E. Bengtsson, Appl. Phys. B, Lasers Opt. **78**, 241 (2004)
55. H.A. Michelsen, M.A. Linne, B.F. Kock, M. Hofmann, B. Tribalet, C. Schulz, Appl. Phys. B, Lasers Opt. **93**, 645 (2008)
56. F. Goulay, P.E. Schrader, L. Nemes, H.A. Michelsen, Mol. Phys. **108**, 1013 (2010)

57. S.-A. Kuhlmann, J. Reimann, S. Will, J. Aerosol Sci. **37**, 1696 (2006)
58. F. Liu, K.J. Daun, D.R. Snelling, G.J. Smallwood, Appl. Phys. B, Lasers Opt. **83**, 355 (2006)
59. H. Michelsen, Appl. Phys. B, Lasers Opt. **94**, 103 (2009)
60. D.R. Snelling, F. Liu, G.J. Smallwood, Ö.L. Gülder, Combust. Flame **136**, 180 (2004)
61. H.A. Michelsen, P.E. Schrader, F. Goulay, Carbon **48**, 2175 (2010)
62. E.A. Rohlfing, J. Chem. Phys. **89**, 6103 (1988)
63. R.J. Santoro, H.G. Semerjian, R.A. Dobbins, Combust. Flame **51**, 203 (1983)
64. R. Puri, T.F. Richardson, R.J. Santoro, R.A. Dobbins, Combust. Flame **92**, 320 (1993)
65. Ü.Ö. Köylü, C.S. McEnally, D.E. Rosner, L.D. Pfefferle, Combust. Flame **110**, 494 (1997)
66. S. Will, S. Schraml, K. Bader, A. Leipertz, Appl. Opt. **37**, 5647 (1998)
67. P. Liu, P.J. Ziemann, D.B. Kittelson, P.H. McMurry, Aerosol Sci. Technol. **22**, 293 (1995)
68. P. Liu, P.J. Ziemann, D.B. Kittelson, P.H. McMurry, Aerosol Sci. Technol. **22**, 314 (1995)
69. X. Zhang, K.A. Smith, D.R. Worsnop, J.-L. Jimenez, J.T. Jayne, C.E. Kolb, Aerosol Sci. Technol. **36**, 617 (2002)
70. X. Wang, P.H. McMurry, Aerosol Sci. Technol. **40**, 320 (2006)
71. R.J. Santoro, J.H. Miller, Langmuir **3**, 244 (1987)
72. H.A. Michelsen, A.V. Tivanski, M.K. Gilles, L.H. van Poppel, M.A. Dansson, P.R. Buseck, Appl. Opt. **46**, 959 (2007)
73. F. Goulay, P.E. Schrader, H.A. Michelsen, In preparation (2009)
74. R.A. Dobbins, C.M. Megaridis, Langmuir **3**, 254 (1987)
75. R.T. Wainner, J.M. Seitzman, S.R. Martin, AIAA J. **37**, 738 (1999)
76. G.D. Yoder, P.K. Diwaker, D.W. Hahn, Appl. Opt. **44**, 4211 (2005)
77. C.B. Stipe, D. Lucas, C.P. Koshland, R.F. Sawyer, Appl. Opt. **44**, 6537 (2005)
78. U. Westblom, P.E. Bengtsson, M. Alden, Appl. Phys., B Photophys. Laser Chem. **52**, 371 (1991)
79. P.-E. Bengtsson, M. Aldén, Appl. Phys. B, Lasers Opt. **60**, 51 (1995)
80. J. Walewski, M. Rupinski, H. Bladh, Z.S. Li, P.-E. Bengtsson, M. Aldén, Appl. Phys. B, Lasers Opt. **77**, 447 (2003)
81. M. Commodo, S. Violi, A. D'Anna, A. D'Alessio, C. Allouis, F. Beretta, P. Minutolo, Combust. Sci. Technol. **179**, 387 (2007)
82. F. Goulay, L. Nemes, P.E. Schrader, H.A. Michelsen, Mol. Phys. **108**, 1013 (2010)
83. E. Therssen, Y. Bouvier, C. Schoemaecker-Moreau, X. Mercier, P. Desgroux, M. Ziskind, C. Focsa, Appl. Phys. B, Lasers Opt. **89**, 417 (2007)
84. R.J. Santoro, T.T. Yeh, J.J. Horvath, H.G. Semerjian, Combust. Sci. Technol. **53**, 89 (1987)
85. R.L. Vander Wal, T.M. Ticich, A.B. Stephens, Combust. Flame **116**, 291 (1999)
86. S. De Iuliis, F. Migliorini, F. Cignoli, G. Zizak, Appl. Phys. B, Lasers Opt. **83**, 397 (2006)
87. F. Goulay, P.E. Schrader, H.A. Michelsen, Appl. Phys. B **100**, 655 (2010)